Article

First Law Optimization and Review of Double and Triple-Effect Parallel Flow Vapor Absorption Refrigeration Systems

Md. Azhar [ID]

Department of Mechanical Engineering, Maulana Mukhtar Ahmad Nadvi Technical Campus, Malegaon 423203, Maharashtra, India; md_azhar@zhcet.ac.in

Abstract: Parallel flow double and triple-effect vapor absorption cooling systems (VACS) are trying to meet the challenges of vapor compression cooling systems due to their better performance. Therefore, the present study deals with the review, thermodynamic analysis, and optimization of operating parameters for both double and triple-effect VACS. Lithium bromide water was selected as the working fluid, while liquified petroleum gas (LPG) and compressed natural gas (CNG) were taken as the source of energy to drive both the VACS. Detailed First Law analysis, i.e., coefficient of performance (COP), was examined along with the optimization of operating parameters (such as salt concentration and operating generators temperature at different pressure levels) and the volume flow rate of the gases. Optimization was carried out for maximum COP of the VACS using an iterative technique. Our results show that the COP of the triple-effect system was approximately 32% higher than the double effect, while 15–20% less consumption of the gases (LPG and CNG) was observed. The most optimum stage for the operation of triple-effect VACS was reached at $T_e = 4\ °C$ and $T_c = T_a = 30\ °C$, $T_g = 180\ °C$, $T_{c4} = 104\ °C$, $T_{c3} = 66\ °C$, $Z_1 = 0.5$, and $Z_2 = 0.45$.

Keywords: triple effect; vapor absorption refrigeration system; parallel flow; thermodynamic analysis; optimization

1. Introduction

VACS are receiving more attention in the published literature as a means of cooling production from different renewable sources, such as solar energy [1], geothermal energy [2], and clean energy [3,4], with many processes switching from energy-intensive vapor compression cooling systems (VCCS). The only drawback of VACS over VCCS is their lower coefficient of performance and high capital investment [5]. However, with development of the systems, current VACS reach the performance of VCCS [6]. The performance of VACS largely depends on the structure (e.g., single to fourth-effect or other) as well as the properties of the working fluids [7]. Mixtures of VACS are environmentally friendly, have less purchasing cost, and are easily available in the market. Additionally, several mixtures have been tested, and a plethora of research has been reported on different suitable mixtures [8]. A few mixtures have been investigated, such as $LiBr/H_2O$ and NH_3/H_2O [9], whereas other ionic liquids [10], inorganic salts [11], and organic [12] have also been examined. Yanbin Qin et al. [13] used low-GWP mixtures R1234yf/R32 and R170/R14/R50 to operate a cooling system integrated with the Linde-Hampson system.

In addition to the mixtures, the flowsheet structure also plays a crucial role in enhancing the performance of VACS [14]. In the past literature, single-effect (SE-VACS) and double-effect VACS (DE-VACS) have been examined exhaustively along with different combinations of the working fluids [15]. Single-effect VACS have very low COPs compared to double and triple-effect VACS (TE-VACS) under different cycle constructions [16]. Talpada and Ramana [17] studied the detailed analysis of DE-VACS. Firstly, the TE-VACS concept was proposed by [18]. A plethora of research has been carried out on the modification of DE-VACS and TE-VACS [19,20]. Rasoul Nikbakhti et al. [21] reviewed in detail the

absorption cooling system for the enhancement of COP. They discussed the different constructions of VACS under multiple effects. Multi-effect VACS have modifications in terms of equipment connectivity and improving operating process performance indicators [22]. T.A. Mouneer et al. [23] performed a thermodynamic analysis of novel VACS integrated with a vapor compression system.

DE-VACS and TE-VACS have two and three generators; therefore, different flow configurations of the working fluids can be possible. The most common working fluid configurations are reverse flow, parallel flow, and series flow [24]. In the previous literature, these flow configurations have been studied in detail [25]. Azhar and Siddiqui [26] presented the thermodynamic analysis of a parallel flow DE-VACS and compared the same system with its series flow configuration. They reported that parallel flow has approximately 6% more COP than series flow VACS. Additionally, they concluded that the rate of exergy destruction for parallel flow VACS is 4% lower, and the energy to drive the system is around 3% lower compared to series flow VACS. Chahartaghi et al. [27] presented two novel arrangements of parallel and series flow DE-VACS. They again concluded that parallel flow VACS have a higher COP. They defined the solution distribution ratio for parallel flow cycles, and these were optimized for maximum COP. Konwar et al. [28] presented a comparison analysis of series and parallel flow VACS. They used two different working fluids, such as water–LiCl and water–LiBr, and optimized the system for maximum COP and minimum irreversibility of both types of VACS. They concluded that the system operated with water–LiCl had lower COP than water–LiBr; however, exergy efficiency was higher at optimized conditions.

Bagheri et al. [29] performed detailed work on the basis of the second Law of Thermodynamics to simulate parallel flow DE-VACS and optimize the performance of maximum COP and exergy efficiency. They reported the maximum COP as 1.295 and maximum exergy efficiency as 22.5% at generator temperatures of 169.6 °C and 142.7 °C, respectively. Both endogenous and exogenous parts of exergy were discussed in their analysis. Exergy is the best tool to determine the location, magnitude, and sources of thermodynamic inefficiencies in any energy conversion devices [30]. Kelly et al. [31] discussed that exergy destruction (irreversibilities) has two components such as endogenous exergy destruction and exogenous exergy destruction. They discussed in detail the importance and application of both parts of exergy for any energy conversion devices, especially vapor absorption refrigeration systems. Garousi et al. [32] conducted a thermodynamic study of all three types of DE-VACS, including reverse parallel flow and parallel and series flow configurations. They discussed the pros and cons of the results of all three configurations of the double-effect VACS. Arshad et al. [33] performed optimization and thermodynamic analysis for series and parallel flow DE-VACS. It was found that the exergy efficiency of parallel flow was 6.45% higher than the series flow configuration under the same operating condition. Detail comparisons have been presented between series and parallel flow systems [33].

Ferwati et al. [34] carried out a detailed thermodynamic analysis of parallel flow double-effect VACS using an H_2O–[mmim][DMP] working pair and compared the system with a conventional H_2O–LiBr pair. It was concluded that the ionic pair had higher COP (around 6%) and ECOP (around 5%) than the H2O–LiBr pair. Arora et al. [35] performed a calculation of energy and exergy of parallel flow DE-VACS and reported the optimum solution distribution ratio (SDR) for maximum COP and maximum ECOP of the system. The optimum temperatures in each component at optimum SDR are reported in their paper. It can be concluded that the SDR also play an important role in the case of the parallel flow absorption–refrigeration cycle. Ahmed and Gilani discussed the performance of a commercial absorption chiller under a double-effect parallel flow arrangement [36]. They presented energy and exergy performance and provided information regarding concentration, temperature, mass flow rate, entropy, and exergy flow at all state points of the systems. However, they failed to optimize all operating parameters under optimum SDR. Garousi et al. [32] performed interesting work to simulate the three flow configurations

(series, parallel, and reverse) of DE-VACS. They discussed the pros and cons in the results of all three configurations of DE-VACS but failed to discuss the same flow configurations of TE-VACS.

The source of energy also affects the exergy performance of VACS. Renewable sources and waste heat become the best option when these sources are available; otherwise, direct-fired sources (such as the burning of fuel in the generator) will meet the requirement of multi-effect VACS when operated at night hours. Zakariya Kaneesamkandi et al. [37] demonstrated an appropriate solar collector for the operation of single and double-effect VACS. A multi-attribute decision-making model was adopted to determine the best option. Mengxiao Yu et al. [38] used industrial low-level waste heat to operate cascade absorption heat transformers and perform multi-objective optimization in terms of energy, exergy, and economic analysis. A different, new configuration of VACS was reported by Gado et al. [39]. They published a detailed review of the hybrid sorption–vapor compression refrigeration system. They presented the integration of a desiccant cooling, adsorption, and absorption system and carried out the energy, exergy, environmental, and economic analysis of the said system. Mengxiao Yu et al. [40] also used low-grade waste heat to operate a cascade absorption refrigeration system and calculate the exergy and exergoeconomic analysis of the said system. Yinglong Wang et al. [41] designed the cascade absorption heat transformer for the recovery of low-grade waste heat. They conducted advanced exergy and exergoeconomic analyses for the said system. Table 1 summarizes the results obtained for parallel flow DE-VACS and TE-VACS in the open literature.

Table 1. Result Summary of parallel flow DE-VACS and TE-VACS.

Type of VACS	Working Fluid(s)	Flow Configuration	Remark on Findings	Reference
Double effect	H_2O–LiBr	Series and Parallel	Comparison between series and parallel flow cycles.	[26]
Double effect	H_2O–LiBr	Series and Parallel	Comparison of parallel flow with series flow and optimized the operating parameters.	[27]
Double effect	Two pairs are used; H_2O–LiBr and H_2O–LiCl	Series and Parallel	Detailed comparison between series and parallel flow.	[28]
Double effect	H_2O–LiBr	Parallel Flow	Detailed exergy analysis and reported maximum COP and their corresponding generator's temperature.	[29]
Double effect	H_2O–LiBr	Series, Parallel, and Reverse Flow	Performance of all three cycles and compared them.	[32]
Double effect	H_2O–[mmim][DMP] and H_2O–LiBr	Parallel Flow	Reported thermodynamic properties of H_2O–[mmim][DMP] mixture.	[34]
Double effect	H_2O–LiBr	Parallel	COP and exergy destruction rate of each component.	[36]
Triple effect	H_2O–LiBr	Series Flow	COP and exergy efficiency and exergy destruction rate of each component.	[7]
Triple effect	NH_3–$LiNO_3$ mixture	Series and Inverse Flow	COP and optimized parameters.	[19]
Triple effect	H_2O–LiBr	Series Flow	COP and optimized temperatures.	[6]
Triple effect	H_2O–LiBr	Series Flow, Parallel, and Reverse Flow	COP, maximum pressure, and maximum temperature of the cycle under different environmental conditions.	[42]

In the open literature, exhaustive work on vapor absorption refrigeration systems has been reported for single-effect to triple-effect cycles. However, the majority of works have reported on series flow configuration. The analysis of parallel flow TE-VACS seems to be missing in the literature and also requires critical review and comprehensive study. However, parallel flow DE-VACS have been discussed in previous studies. In contrast, a few works have been reported on the direct-fired arrangement in the main generator. It is known that DE-VACS and TE-VACS operated at significantly higher generator temperatures can be achieved easily through the direct-fired arrangement. In view of this, the present study has addressed the following research gaps:

1. Review of DE-VACS and TE-VACS under different flow configurations and different heat sources.
2. Detailed energy analysis for parallel flow TE-VACS.
3. A direct-fired system has been selected for the operation of the main generator. Moreover, LPG and CNG have been taken as sources of energy because they are cheaper, less toxic, and easily available.
4. Calculation of gases required to operate the parallel flow DE-VACS and TE-VACS.
5. Optimization of operating temperature and SDRs for maximum COP.

2. System Description of VACS

Here, the modeling and working principle of both parallel flow DE-VACS and TE-VACS are discussed in detail.

2.1. Parallel Flow DE-VACS

A schematic diagram of a typical parallel flow DE-VACS is shown in Figure 1a. The absorber, evaporator, main condenser, main generator, and condenser–generator set (i.e., C3-G2) are the major parts of DE-VACS. The working of parallel flow DE-VACS is quite simple and discussed in detail by Azhar and Siddiqui [43]. In this system, the input energy is supplied only in the main generator; the other generator (G2) is operated with internal heat recovery by condenser 'C3'. Refrigerant is generated in both generators simultaneously. The solution is divided into both generators after the absorber outlet. Initially, the solution (combination of refrigerant and absorbent) is prepared in the absorber and pumped to both generators through the preheater. In both generators, the solution is heated, and the refrigerant vapor that has been collected is released in the main condenser and transfers the phase from vapor to liquid. The liquid refrigerant is sent to the evaporator via a throttle valve. In the evaporator, the refrigerant boils and takes heat from the cooled space and then sends it to the absorber to make it a cyclic process.

2.2. Parallel Flow TE-VACS

A schematic plot of parallel flow TE-VACS is depicted in Figure 1b. The working principle is quite similar to parallel flow DE-VACS. However, in this arrangement, there are three generators; therefore, the solution is distributed in two places. Firstly, the solution is divided at the outlet of preheater 1 (i.e., PH1) and then again distributed at the outlet of preheater 2 (i.e., PH2). The refrigerant vapor is generated in all three generators and finally merged in condenser 'C'. However, the remaining strong solution (the solution prepared after boiling the refrigerant) flows back to the absorber to complete the cycle. In the same way, the main generator is driven by the external heat source, while the other two are operated through internal heat recovery (G3 is operated through C4, and G2 is operated through C3). The cooling effect is produced at the evaporator.

Figure 1. (**a**) Schematic plot of direct-fired parallel flow DE-VACS. (**b**) Schematic plot of direct-fired parallel flow TE-VACS.

3. System Modeling

To evaluate the thermodynamic performance of DE-VACS and TE-VACS, the energy balance for all components must be written through the below expression:

$$\text{Mass balance: } \sum\nolimits_{in} \dot{m} - \sum\nolimits_{out} \dot{m} = \frac{dm_{cv}}{dt}, \tag{1}$$

$$\text{Energy balance : } \dot{E}_{in} - \dot{E}_{out} = \frac{dE_{system}}{dt}. \tag{2}$$

After referring to Figures 1 and 2, the expression for different components can be written under steady-state conditions:

$$\text{Absorber : } \dot{m}_7 h_7 + \dot{m}_{10} h_{10} + \dot{m}_{11} h_{11} - \dot{m}_1 h_1 - \dot{m}_{12} h_{12} = 0, \tag{3}$$

$$\text{Solution pump : } \dot{m}_1 h_1 - \dot{m}_2 h_2 + W_{pump} = 0, \tag{4}$$

$$\text{Evaporator : } \dot{m}_6 h_6 + \dot{m}_{17} h_{17} - \dot{m}_7 h_7 - \dot{m}_{18} h_{18} = 0, \tag{5}$$

$$\text{Main generator : } \dot{m}_3 h_3 + \dot{m}_{13} h_{13} - \dot{m}_4 h_4 - \dot{m}_8 h_8 - \dot{m}_{14} h_{14} = 0. \tag{6}$$

For DE and TE-VACS, the equations shall be different for a few components.
Parallel Flow DE-VACS (see Figure 1):

$$\text{Condenser 'C' : } \dot{m}_{4b} h_{4b} + \dot{m}_{4c} h_{4c} + \dot{m}_{15} h_{15} - \dot{m}_5 h_5 - \dot{m}_{16} h_{16} = 0. \tag{7}$$

Generator-Condenser set (G2-C3):

$$\dot{m}_4 h_4 + \dot{m}_{2d} h_{2d} - \dot{m}_{4a} h_{4a} - \dot{m}_{4c} h_{4c} - \dot{m}_{8c} h_{8c} = 0, \tag{8}$$

$$\text{SDR : } Z = \frac{m_{2b}}{m_{2a}} = \frac{m_{2b}}{m_1}.$$

Concentration at 8d:

$$X_{8d} = \frac{1.0}{(Z/X_g) + (1.0 - Z)/X_{gs}}. \tag{9}$$

Parallel Flow TE-VACS (see Figure 2):

$$\text{Condenser 'C' : } \dot{m}_{4b} h_{4b} + \dot{m}_{4c} h_{4c} + \dot{m}_{15} h_{15} - \dot{m}_5 h_5 - \dot{m}_{16} h_{16} = 0. \tag{10}$$

Generator–condenser set G3 and C4:

$$\dot{m}_4 h_4 + \dot{m}_{2h} h_{2h} - \dot{m}_{4a} h_{4a} - \dot{m}_{4c} h_{4c} - \dot{m}_{8c} h_{8c}. \tag{11}$$

Generator–condenser set G2 and C3:

$$\dot{m}_{4b} h_{4b} + \dot{m}_{4c} h_{4c} + \dot{m}_{2d} h_{2d} - \dot{m}_{4d} h_{4d} - \dot{m}_{4f} h_{4f} - \dot{m}_{8g} h_{8g} = 0. \tag{12}$$

Solution distribution ratio:

$$Z_1 = \frac{\text{solution entering in PH2}}{\text{solution leaving from PH1}} = \frac{m_{2b}}{m_{2a}}, \; Z_2 = \frac{\text{solution entering in main generator}}{\text{solution leaving from PH2}} = \frac{m_{2f}}{m_{2e}}. \tag{13}$$

LiBr–salt concentration:

$$X_{J1} = X_{8d} = \frac{1.0}{(Z_2/X_g) + (1.0 - Z_2)/X_{g3}}, \; X_{J2} = X_{8h} = \frac{1.0}{(Z_2/X_g) + (1.0 - Z_2)/X_{g3}}, \tag{14}$$

$$COP = \frac{Q_e}{Q_g + W_p} \tag{15}$$

where

$$Q_e = \dot{m}_7 h_7 - \dot{m}_6 h_6 = \dot{m}_{18} h_{18} - \dot{m}_{17} h_{17} \text{ and } Q_g = \dot{m}_4 h_4 - \dot{m}_3 h_3 + \dot{m}_8 h_8 = \dot{m}_{14} h_{14} - \dot{m}_{13} h_{13}.$$
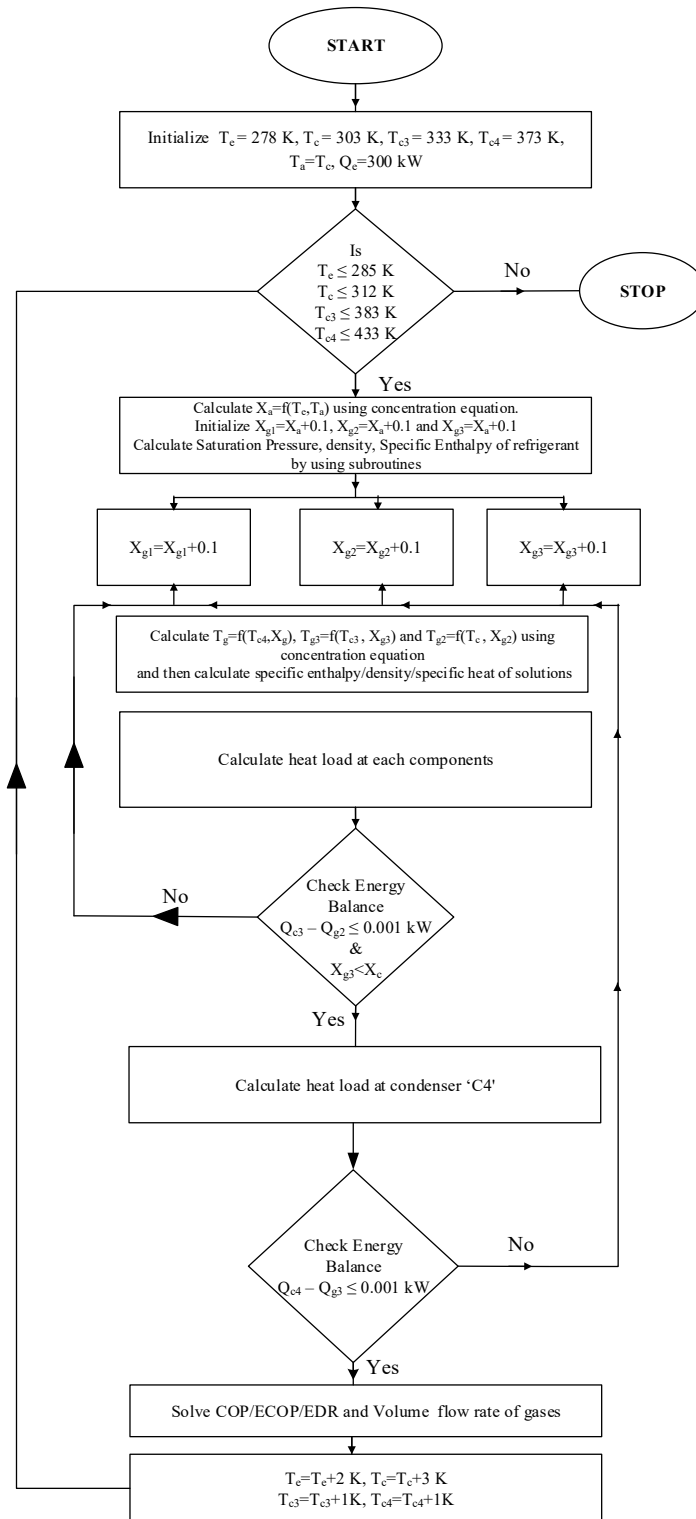

Figure 2. Flow chart for the triple-effect parallel flow cycle.

3.1. Modeling of Energy Sources (LPG and CNG)

In the present work, the two gases were selected as the source to operate the main generator of the VACS. These gases are eco-friendly, economical, and less toxic. The detailed calculation of the volume flow rate of each gas was carried out in previous articles [6,44]. Here, only heat release is written through each gas, such as CNG (Q_C) and LPG (Q_L) and their volume flow rate (V_{fuel}):

$$Q_L = 51,615.8 - 17.68 \times (T_p + 273.15) - 2.52 \times 10^{-3} \times (T_p + 273.15)^2, \quad (16)$$

$$Q_C = 53,364.84 - 18.87 \times (T_p + 273.15) - 2.0 \times 10^{-3} \times (T_p + 273.15)^2, \quad (17)$$

$$V_{fuel} = \frac{Q_g}{Q_{fuel}} \times v_{gas}; \, m^3 s^{-1}. \quad (18)$$

For different gases such as CNG and LPG, Equation (18) will change accordingly.

3.2. Assumption and Solution Technique of the Present Work

In the present manuscript, certain assumptions were taken from [45], who simplified the simulation under steady-state conditions. Table 2 shows the operating conditions for the simulation of DE-VACS and TE-VACS. LiBr–water solution and refrigerant properties are taken from [46–48]. To execute the simulation of both DE-VACS and TE-VACS, computer codes were developed and written in FORTRAN 90. The calculation process is very simple, first considering fixed parameters described in Table 2. The generator concentration is increased in the loop, and the generator temperature is calculated with the help of the respective condenser temperature. After that, heat loads at the main generator and intermediate condenser are calculated. This calculation is repeated with increasing values of LiBr concentration of both the generator, which makes the energy balance between the intermediate generator and condenser lie within an error of $\pm$ 0.1 kJ/h. The coefficient of performance and volume flow rate of both gases are estimated for different values of the main generator temperature for fixed values of T_e and $T_c = T_a$. For clarity of the calculation process, the algorithm of the program is shown in Figure 2.

Table 2. Fixed operating conditions for DE-VACS and TE-VACS.

Properties	Values
Evaporator Load	300 kW
Evaporator Temperatures (T_e)	4, 6, 8 and 10 °C
T_{cold}	T_e + 5.0
Absorber/main condenser temperatures	30, 33, 36 and 39 °C
Intermediate condenser/generator temperature, T_{c3}	From 45 °C to 105 °C
Intermediate condenser/generator temperature, T_{c4}	70 °C to 135 °C
Pump Efficiency, η_p, and Effectiveness, ε	85% and 70%
Z, Z_1, and Z_2	0.1–0.7

4. Result and Discussion

LiBr–salt concentration plays an important role in the generator temperature and, ultimately, the performance of VACS. In view of this, the variation in salt concentration must be depicted. Figure 3 shows the variations in absorber concentration (X_a), all generator concentrations (X_g, X_{g2}, and X_{g3}), and crystallization concentration (X_c) with T_g at different T_e of DE-VACS and TE-VACS. In Figure 3, all the condenser temperatures are fixed (T_{c4} = 110 °C T_{c3} = 65 °C and $T_c = T_a$ = 30 °C), and the SDR of DE-VACS is Z = 0.36, while in triple effect, it is Z_1 = 0.3 and Z_2 = 0.5. It is observed from the plots of Figure 3 that X_a remains constant with the increase in T_g. The concentration of LiBr–H_2O solution

in the absorber is the function of the saturation temperature (T_e) of the refrigerant vapor and LiBr–H_2O solution temperature (T_a). Therefore, with the rise in T_e, the values of X_a decrease, while on increasing the temperature T_a, the values of X_a increase. In DE-VACS, the salt concentration of generator G2 (X_{g2}) is lower than the salt concentration in the main generator (X_g), which is unlike the result obtained in series flow DE-VACS [43]. This is because the solution entering both generators has the same concentration (that is, X_a), and, generator G operates at a higher temperature; as a result, higher heat is supplied to it compared to generator G2. This is why more refrigerant vapor is generated in the main generator compared to generator G2. A similar effect is observed in the parallel flow TE-VACS cycle: $X_g > X_{g2} > X_{g3}$, which is again unlike the result obtained for series flow TE-VACS [7].

Additionally, LiBr–H_2O solution coming from generators G and G2 mix at state point 8d in parallel flow DE-VACS, while in TE-VACS, the solutions mix at state points 8d and 8h, respectively. The LiBr–salt concentration at state point 8d (X_{8d}) lies between Xg and X_{g2} in the case of parallel flow DE-VACS. Similarly, in the case of TE-VACS, the LiBr–salt concentration at state point 8d (X_{8d}) will lie between X_g and X_{g3}, while at 8h (X_{8h}) it will lie between X_{g2} and X_{g3}, respectively. The LiBr–salt concentration at different mixing points (that is, X_{8d} and X_{8h}) is shown in Figure 4. Additionally, the salt concentration X_{8d} of DE-VACS and X_{8h} of TE-VACS have the same trend because they exit at the same location of their respective cycles. The trend of the salt concentration at state point X_{8d} (parallel flow TE-VACS) is the same as found for X_{g2}. Moreover, with an increase in the evaporator temperature, the operating range of the LiBr–salt concentration of each generator increases.
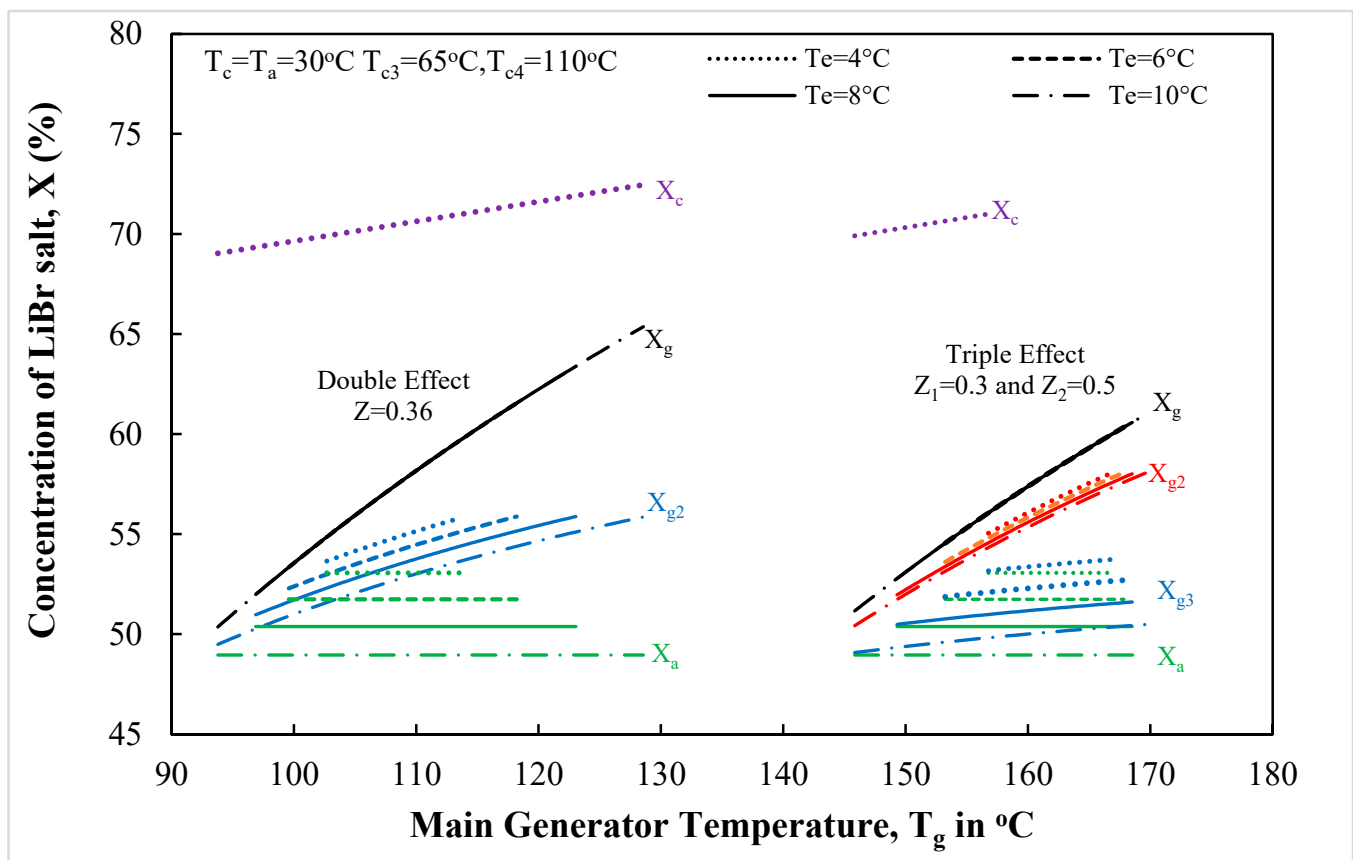

Figure 3. Variation in LiBr–salt concentration at different locations of parallel flow DE-VACS and TE-VACS with T_g.
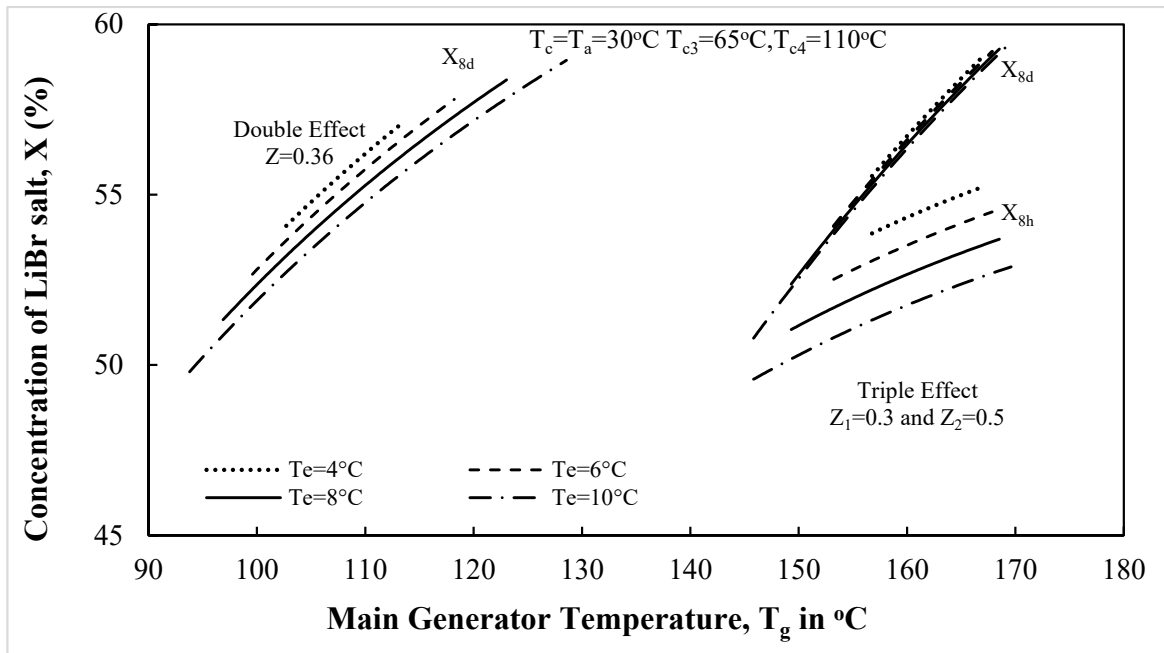
Figure 4. Variation in concentration of the LiBr–salt at mixing points of DE-VACS and TE-VACS with T_g at different T_e.

4.1. Coefficient of Performance

The variation in COP of DE-VACS and TE-VACS with T_g is shown in Figure 5. The intermediate condensers temperature in both cycles is $T_{c3} = 65$ °C (for DE-VACS and TE-VACS), $T_{c4} = 110$ °C (for TE-VACS), and the main condenser temperature $T_c = T_a = 30$ °C is fixed. The SDR in parallel flow DE-VACS is taken as $Z = 0.36$, while in parallel flow TE-VACS it is $Z_1 = 0.3$ and $Z_2 = 0.5$. However, T_e is varied from 4 °C to 10 °C.
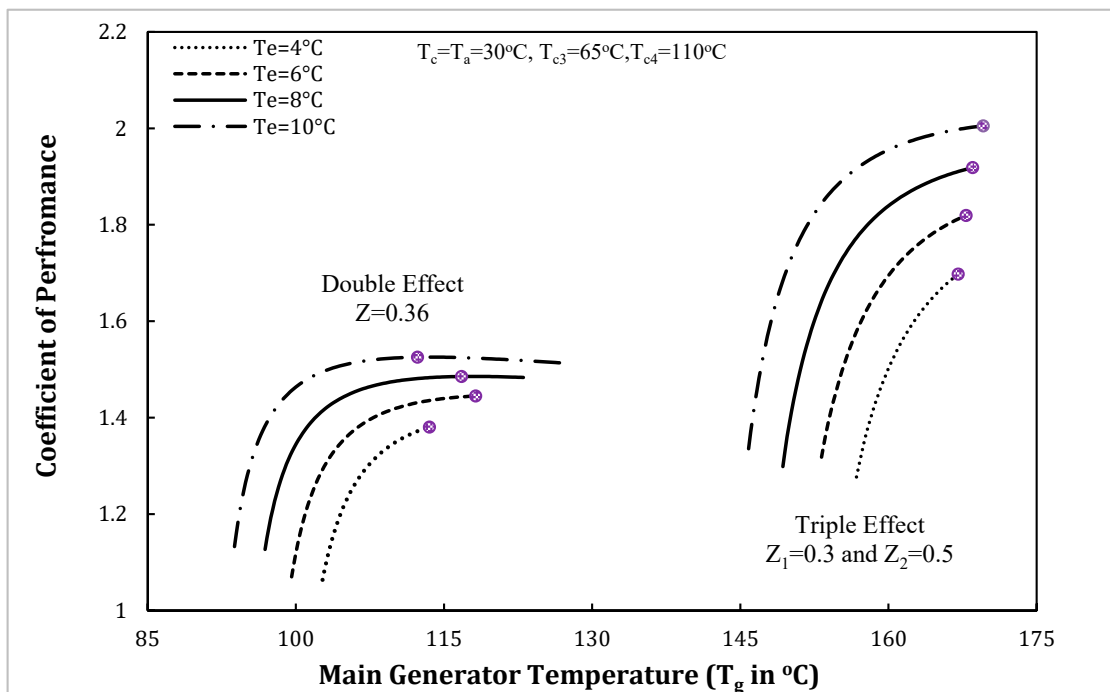
Figure 5. Variation in COP with T_g in DE-VACS and TE-VACS (all SDRs and generators temperatures are fixed).

It is observed from Figure 5 that the values of COP initially increase with the rise in T_g and reach a maximum. This is due to a decline in the generator load for fixed Q_e and T_e. With further increase in T_g, COP terminates because the system must have either faced crystallization or energy balance must be attained in the condenser–generator set(s). Additionally, with a decrease in the values of T_e, the COP of both systems decreases. Maximum COP for SDRs and fixed temperatures are marked with circles in Figure 5. Furthermore, the COP of TE-VACS is significantly higher than that of DE-VACS.

4.2. LPG and CNG Flow Rate

The flow rates of LPG and CNG with T_g for parallel flow DE-VACS and TE-VACS are depicted in Figure 6. It is observed that the LPG and CNG volume flow rate of both VACS decreases with a rise in T_g, attaining a minimum value and then becoming constant due to crystallization or energy balance between the condenser and generator sets. Further, it is also observed that the flow rate of LPG and CNG declines with a rise in the T_e and the minimum flow rate shift towards low T_g. At high T_e, the concentration in the absorber becomes low, which provides a large operating range of the main generator temperature. It is further observed that the flow rate of TE-VACS is lower compared to DE-VACS; the COP of TE-VACS is higher than the COP of DE-VACS. The trends of the gas flow rate are exactly the reverse of variation in the COP.
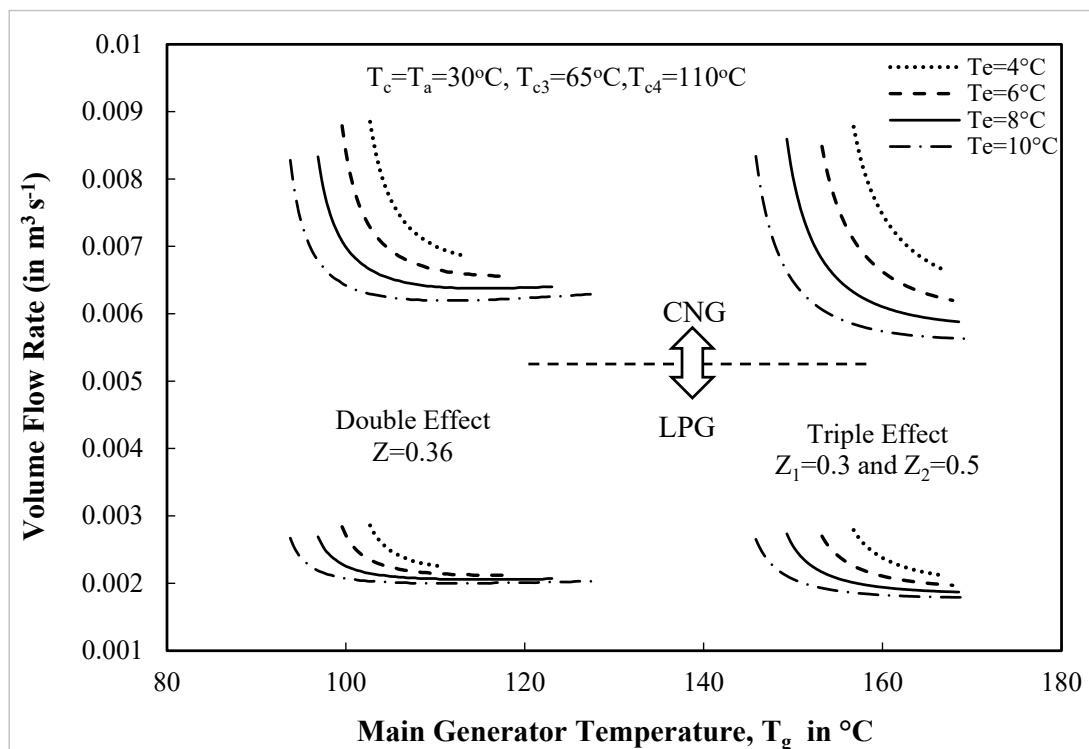

Figure 6. LPG and CNG volume flow rates with T_g.

It was observed through the literature that the operation of VACS is affected by generator temperature; therefore, it is necessary to use all temperatures of the generator(s) to attain high performance. Furthermore, SDRs also affect VACS performance in the case of parallel flow configuration; therefore, optimization of SDR of parallel flow DE-VACS was discussed by Azhar and Siddiqui [43] in detail. However, the optimization of parallel flow TE-VACS needs more clarification, which has not yet been discussed in the open literature. Parallel effect TE-VACS have two SDRs (Z_1 and Z_2), which are also to be optimized for the best performance of the system (i.e., maximum COP/minimum flow rate). For clarity, the optimization procedure is shown in four simple steps.

In the first step of optimization, COP variation with T_g is shown for different values of Z_2 in Figure 7, keeping the evaporator and all the condenser temperatures constant at $T_{c4} = 110\ °C$, $T_{c3} = 65\ °C$, $T_c = T_a = 30\ °C$, and $T_e = 4\ °C$; SDR $Z_1 = 0.3$ must also be constant. It was found that for each value of Z_2, COP increases and then attains a maximum point that has been circled in the same Figure 7. It can be observed that the system operates at lower T_g when Z_2 is low. Moreover, when Z_2 increases, maximum COP also increases (up to 0.2 to 0.4) and then declines. It is also noticed that shifting the maximum values of COP shift towards lower T_g. Finally, from Figure 7, it was observed that the maximum of maximum COP is attained at $Z_2 = 0.4$ for fixed intermediate condenser temperatures and when $Z_1 = 0.3$.

Similarly, in the second step of optimization, SDRs Z_1 and Z_2 are varied, keeping other parameters ($T_{c3} = 65\ °C$ and $T_{c4} = 110\ °C$) constant. Figure 8a shows the variation in maximum COP with Z_2 for different values of Z_1 and selects a maximum of the maximum COP. Rise in Z_1 and keeping Z_2 constant produces a similar effect as deliberated in the first step of optimization. It is observed from Figure 8a that the COP of VACS initially increases, attains a maximum, and then decreases slowly. It is also noticed that the rise in the Z_1 curve slightly flattens and increases, and the COP peak increases up to $Z_1 = 0.55$; after that, the curve flattens more, and COP also decreases.

The maximum of maximum COP has been circled, and both Z_1 and Z_2 are optimized in this step; other parameters that must be optimized in the coming step of optimization remain constant. For clear visibility of the results in Figure 8a, the optimum values of Z_2 and COP obtained from Figure 8a are shown in the form of bars in Figure 8b.
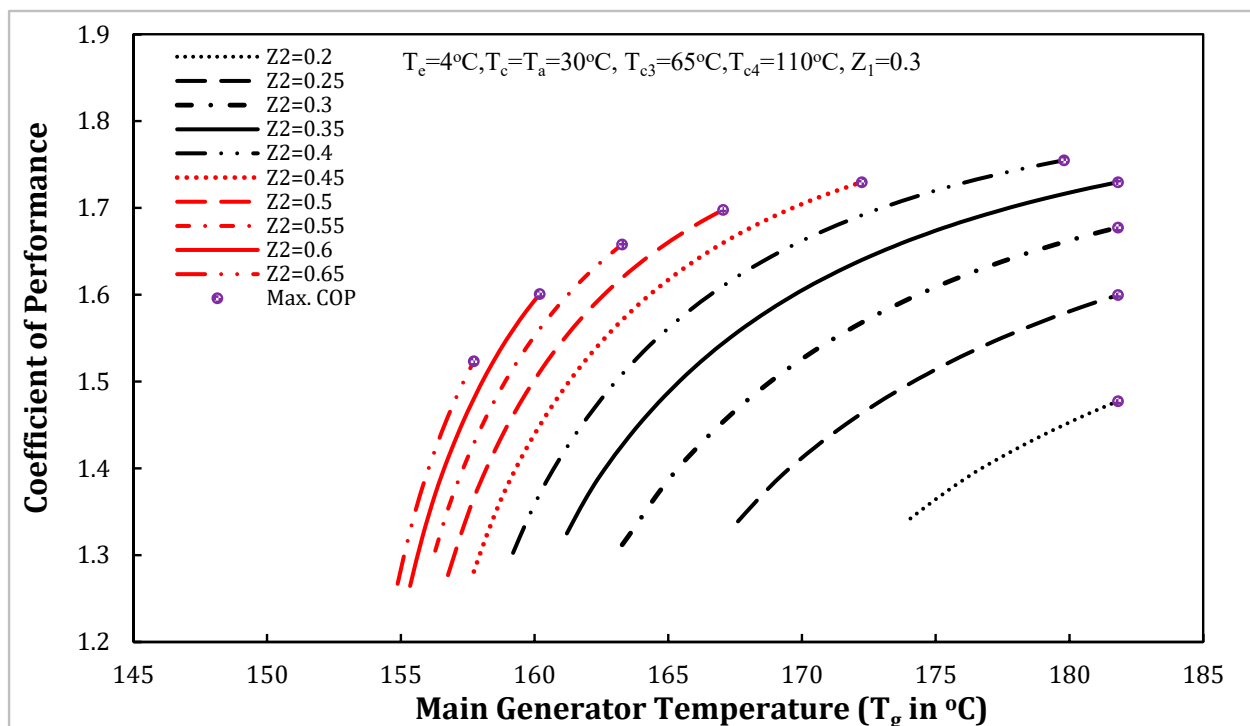

Figure 7. COP with T_g for different Z_2 (Z_1 and all generator temperatures are fixed).

From Figure 8a,b, it can be noticed that the maximum value of COP is attained at $Z_1 = 0.5$ and $Z_2 = 0.4$, keeping $T_{c3} = 65\ °C$ and $T_{c4} = 110\ °C$ as constant. In the coming step, the intermediate temperatures must be optimized. Figure 9a optimized the temperature T_{c4} and presented the variation in COP with Z_1, Z_2, and T_{c4}. Again, the same method was adopted for optimization, and the code was run for different values of T_{c4}. It was observed that at each value of T_{c4}, COP initially rise, attains a maximum point, and then decreases.
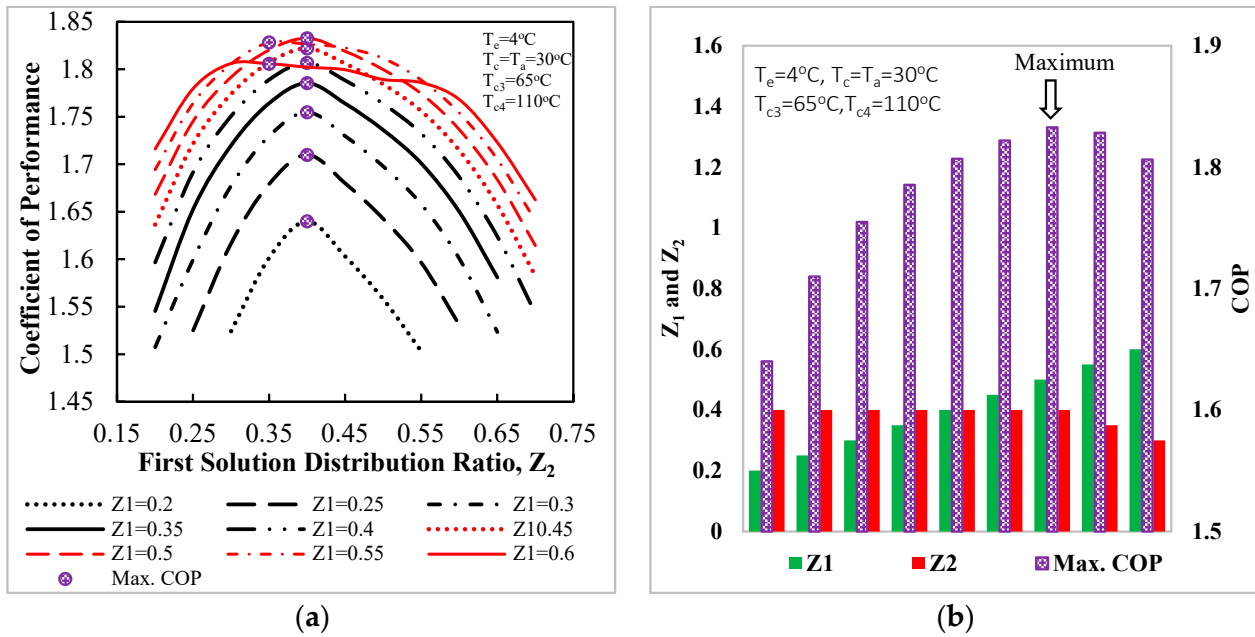
Figure 8. (**a**) Variation in COP with Z_2 for different Z_1. (**b**) Optimum values of Z_2 and COP for different Z_1.

At this stage, the intermediate condenser temperature T_{c4} is optimized along with both SDRs. Again, for more clarity of the results, the optimum values of Z_1, Z_2, and COP at each T_{c4} are shown in the form of bars in Figure 9b. The maximum COP attained in Figure 9a,b is at $T_{c4} = 114$ °C, $Z_1 = 0.45$, and $Z_2 = 0.45$ for fixed $T_{c3} = 65$ °C. Further, the variation in maximum COP and optimum Z_1 and Z_2 with T_{c4} and T_g is shown in Figure 10a,b. It is thus very interesting to see that as COP increases with T_{c4}, Z_2 increases while Z_1 decreases simultaneously. In Figure 10a, it is also found that both SDRs meet at a certain value of T_{c4} where the COP is near the maximum value. The same is the case with T_g in Figure 10b.
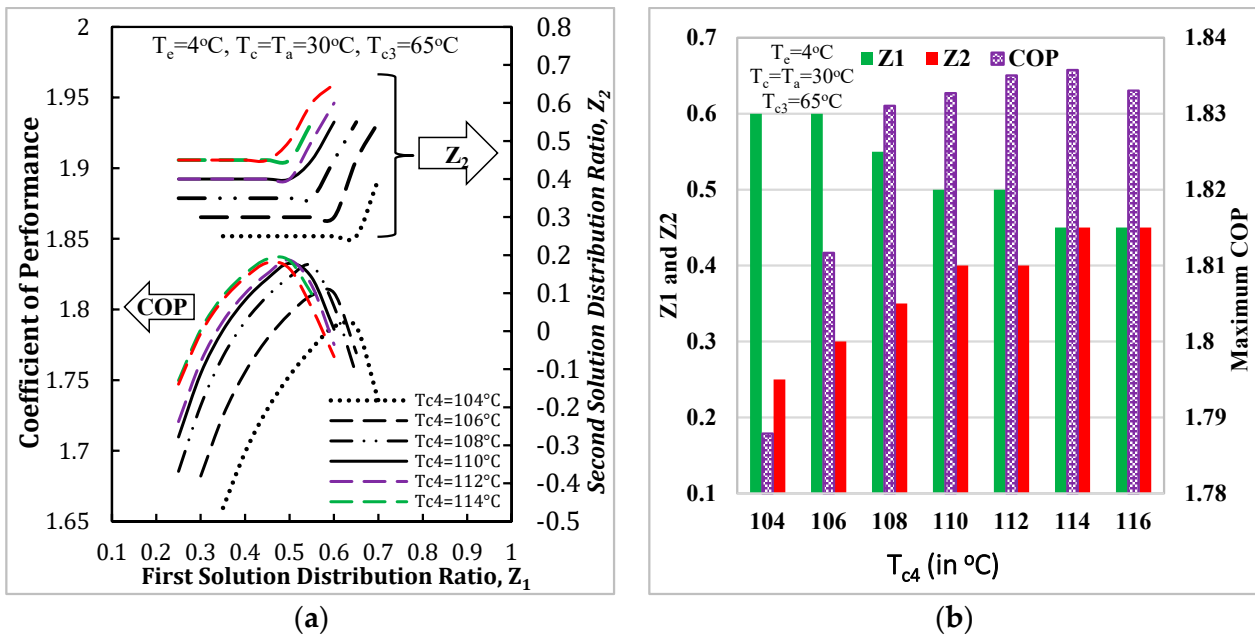

Figure 9. (**a**) COP and Z_2 with Z_1 for different T_{c4} temperatures. (**b**) Optimum values of Z_1, Z_2, and COP from (**a**).
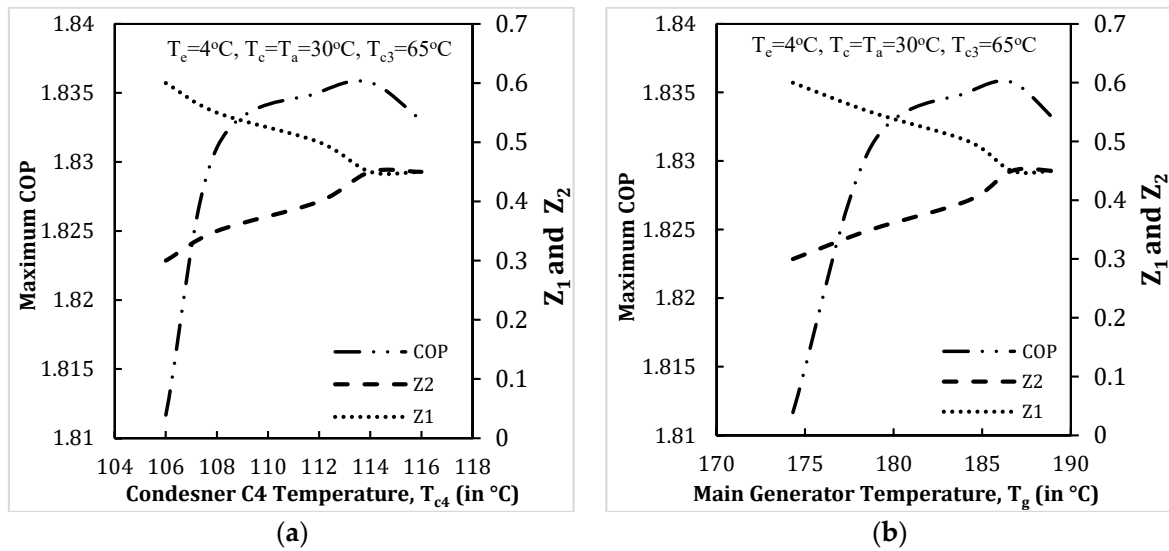
Figure 10. Maximum COP, Z_2, and Z_1 with temperatures T_{c4} (**a**) and T_g (**b**).

In the fourth step of optimization, the aim is to optimize the intermediate condenser/generator temperature T_{c3} for higher performance. The method that was selected to optimize the other parameters Z_1, Z_2, and T_{c4} was repeated for different values of T_{c3}. At each T_{c3}, we obtained the maximum of the maximum COP that is noted and plotted in Figure 11 in bars form. It was also observed that maximum COP was achieved at $T_{c3} = 66\,°C$, and correspondingly, all other optimized parameters were noted down. In Figure 12, all the optimized generator temperatures were plotted with COP. The method of optimization used to optimize all the operating parameters was the iterative technique. The computer code was run for different values of Z_1, Z_1, T_{c4}, and T_{c3}, the maximum COP was selected in each case, and finally, the most optimum value was obtained so that the design engineers could work on the same values for the fixed evaporator and main condenser/absorber temperatures. It should be clear that the all-optimum values will change once the evaporator and main condenser/absorber temperatures change. From Figure 12 it is shown that the most optimum stages reached at $T_e = 4\,°C$ and $T_c = T_a = 30\,°C$ are $T_g = 180\,°C$, $T_{c4} = 104\,°C$, $T_{c3} = 66\,°C$, $Z_1 = 0.5$, and $Z_2 = 0.45$.
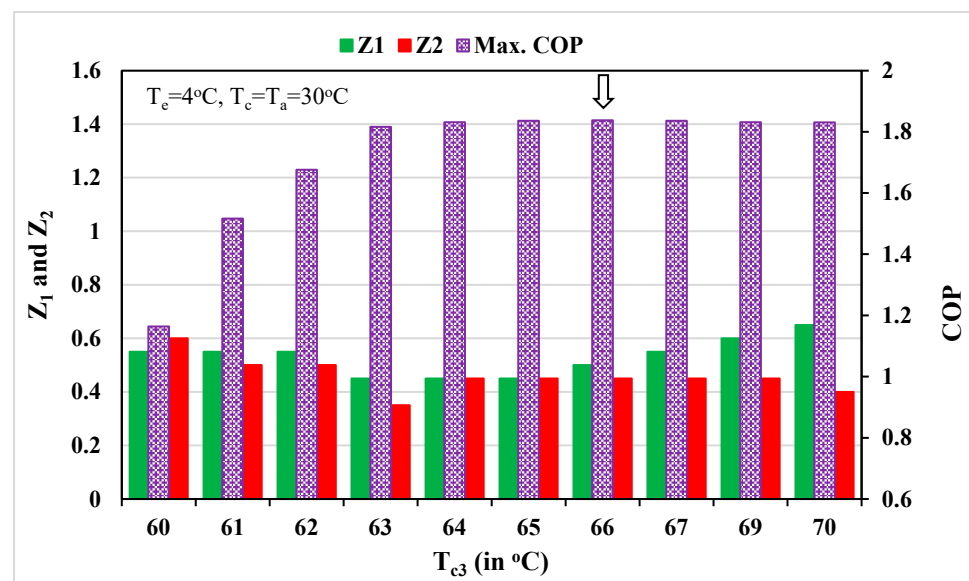

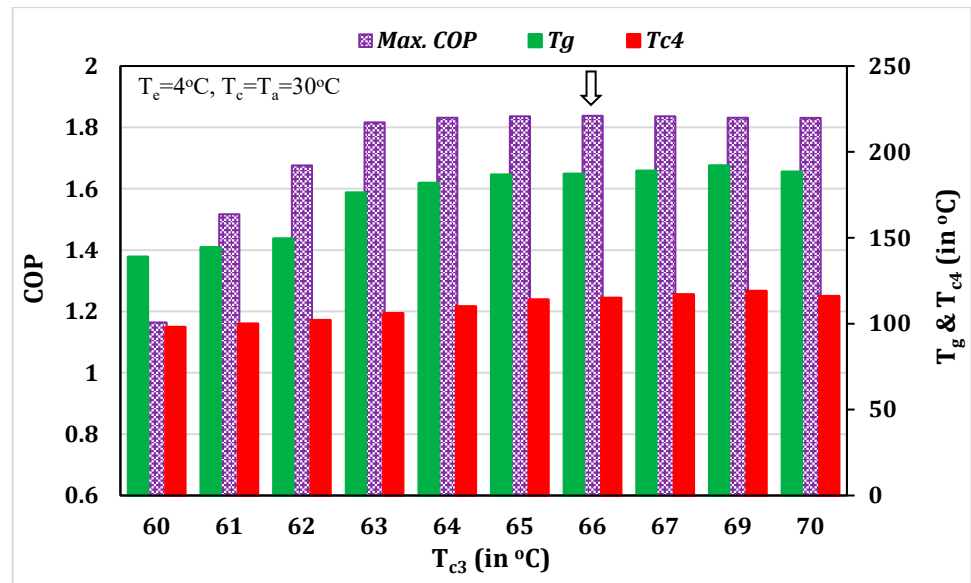**Figure 11.** Maximum COP with T_{c3} under different Z_1 and Z_2.

Figure 12. Maximum COP, T_g, and T_{c4} with temperature T_{c3}.

Now, for different values of T_e, the variation in maximum COP with T_g is shown in Figure 13a, keeping $T_c = T_a = 30\ ^\circ C$ fixed, yet all the operating parameters (all generator temperature and SDRs) at this stage are optimized. Similar plots can also be drawn for other values of $T_c = T_a$. It is also seen that COP increases with an increase in T_e and shifts towards lower generator temperature. The optimum COP for each T_e is marked with a circle, which is the optimum operating condition for parallel flow TE-VACS. Additionally, the optimum COP at each T_e is shown in the form of bars in Figure 13b. Furthermore, the operating temperature in all three generators at different values of T_e is shown in Figure 14. The main generator (T_g) has a very high temperature, and the generator G3 has a somewhat lower temperature (T_{g3}) than T_g. The generator G2 required a lower temperature (T_{g2}) than T_{g3}. All the generators showed decreasing temperature with an increase in T_e which is obvious.
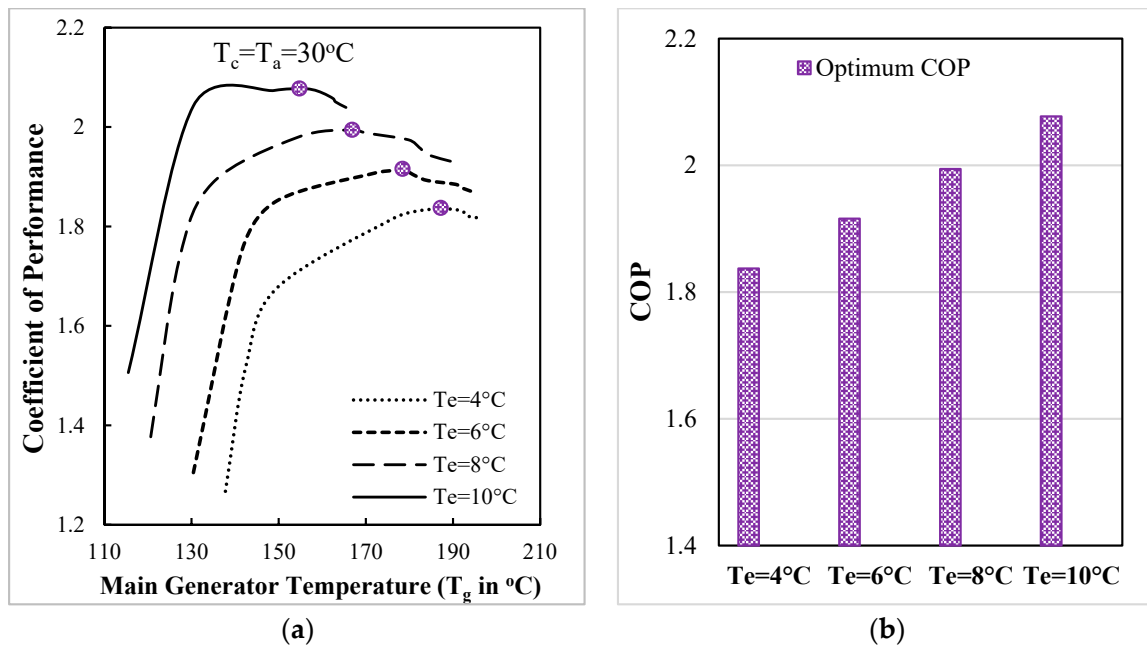

(a)

(b)

Figure 13. (**a**) COP with T_g for different values of T_e. (**b**) Optimum COP for different values of T_e (all parameters are optimized).
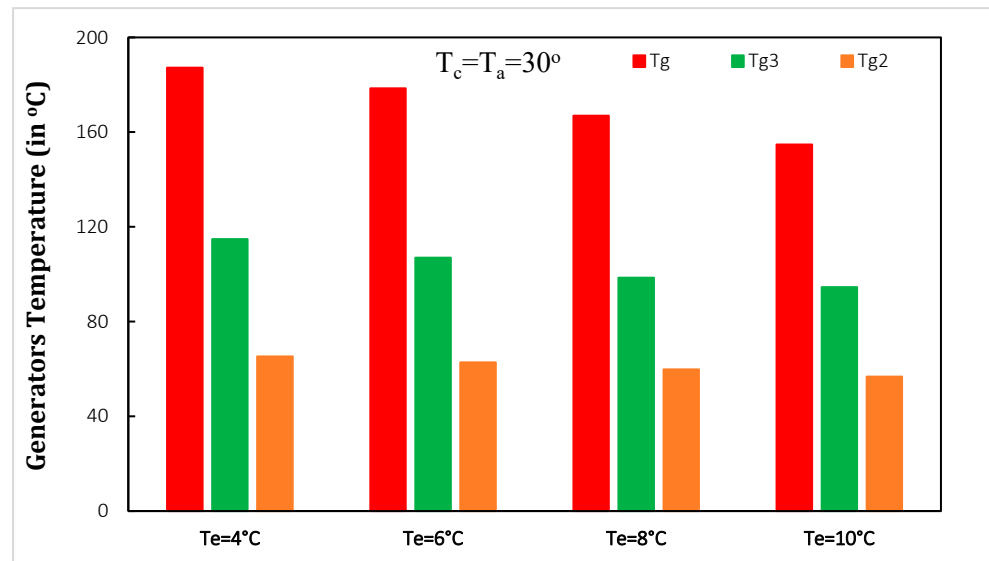
Figure 14. Optimum generator temperatures at different evaporator temperatures (all operating parameters are optimized).

Figure 15 demonstrates a comparison study between DE-VACS and TE-VACS for $T_e = 4$ °C and 10 °C, with $T_c = T_a = 30$ °C as fixed values. Additionally, the plots in Figure 15 were drawn after the optimization of operating parameters in both cycles. Here, a similar trend is found for COP, which initially increases, reaches a maximum, and then decreases. The comparison shows that the COP of parallel flow TE-VACS is approximately 32% higher than that of parallel flow DE-VACS. Furthermore, with an increase in T_e, COP increases, and the optimum values of COP at higher T_e shift towards lower T_g.
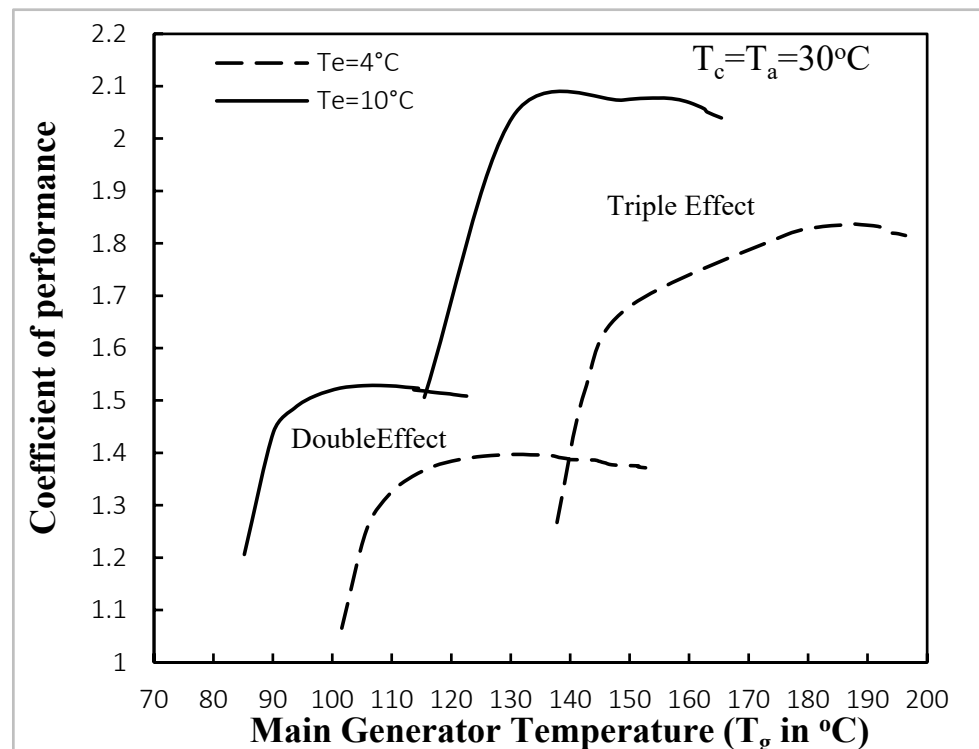

Figure 15. Maximum COP of DE-VACS and TE-VACS.

After the optimization of the solution distribution ratio and temperatures in the main generator and intermediate generator/condenser, CNG and LPG volume flow rates are determined with the help of Equation (18). The flow rate of CNG and LPG of both cycles are presented and compared in Figure 16 for T_e = 4 °C and T_c = T_a = 30 °C. It is seen that the flow rate of CNG is significantly higher than that of LPG due to the difference in their specific volume. The specific volume of CNG is higher than that of LPG. Additionally, the minimum flow rate of LPG and CNG obtained correspond to the maximum COP in the present analysis. Furthermore, the minimum flow rate obtained for parallel flow cycles at each T_e lies at a higher T_g than the series flow cycle. Therefore, it is inferred that parallel flow cycles have higher COP and lower gas requirements than series flow cycles, but they need high heat source temperatures.
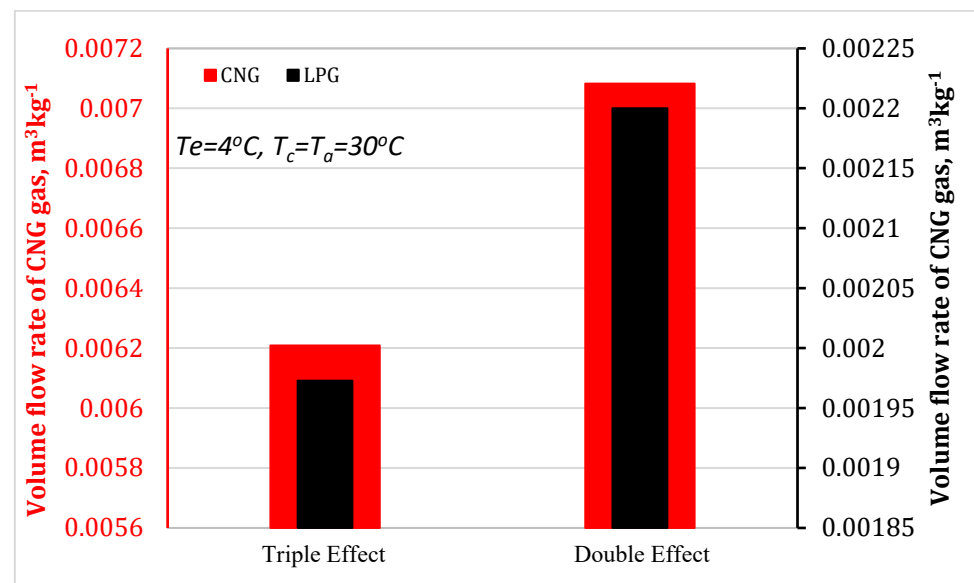

Figure 16. Comparison of minimum LPG and CNG volume flow rate of DE-VACS and TE-VACS.

5. Conclusions

In the present communication, first, a brief review was conducted on VACS under different constructions and flow configurations. Additionally, parallel flow TE-VACS were simulated, exploring the optimum operating parameters such as temperature and SDRs. The comparison of DE-VACS and TE-VACS is presented for different T_e and T_c = T_a. The following observations and conclusions made from the present work are listed below:

i.   For the purpose of saving high-grade energy, VACS have become quite popular recently and have been made more efficient through a plethora of studies. This review shows that current VACS are more efficient and environmentally friendly.

ii.   From the literature review, it was also observed that the working fluid flow configuration produces a high impact on the performance of VACS.

iii. The temperature of the intermediate generator also plays a vital role in the performance of DE-VACS and TE-VACS under different flow configurations.

iv.   TE-VACS have around 32% higher performance than DE-VACS, while they require 15–20% less consumption of gases (LPG and CNG) to operate the system.

v.   As the generator temperature plays an important role in the performance of TE-VACS, T_g, T_{g2} ($\approx T_{c3}$), and T_{g3} ($\approx T_{c4}$) are reported for maximum COP and minimum flow rates of the gases.

vi.   In parallel flow cycles, SDR(s) is/are also an important factor in deciding the performance optimized for maximum COP and minimum flow rate of the gases.

vii.   For T_e = 4 °C and T_c = T_a = 30 °C, the optimum condition to run TE-VACS is T_g = 180 °C, T_{c4} = 104 °C, T_{c3} = 66 °C, Z_1 = 0.5, and Z_2 = 0.45. These values can be changed after changing the evaporator and condenser temperature.

viii.   Similarly, the optimum flow rate for the fixed evaporator and condenser temperatures are 0.0022 (for DE-VACS) and 0.00197278 (for TE-VACS) for LPG, while for CNG the values are 0.007082 (for DE-VACS) and 0.00620872 (for TE-VACS). These values will help engineers who are working in the field of absorption refrigeration systems. This is one of the key findings of the present manuscript.

Conflicts of Interest: The author declares no conflict of interest.

Nomenclature

A	absorber
C	main condenser
COP	coefficient of performance [-]
CNG	compressed natural gas
E	evaporator
G	generator at which heat is supplied
h	specific enthalpy [kJ kg^{-1}]
LPG	liquefied petroleum gas
LiBr	lithium bromide salt
$\dot{m}$	rate of mass flow [kg s^{-1}]
P	pressure [kPa]
Q	heat transfer rate [kJ s^{-1}]
Q_C	energy from CNG [kJ kg^{-1} CNG]
Q_L	energy from LPG [kJ kg^{-1} LPG]
T	temperature [°C]
T_{cold}	cooled space temperature
TV	throttle valve
V	gas flow rate [m^3 s^{-1}]
W_p	pump work [kW]
Greek Symbols:	
Subscripts:	
a	absorber
c	main condenser
e	evaporator
g	main generator

References

1.   Meraj, M.; Khan, M.E.; Azhar, M. Performance analyses of photovoltaic thermal integrated concentrator collector combined with single effect absorption cooling cycle: Constant flow rate mode. *J. Energy Resour. Technol. Trans. ASME* **2020**, *142*, 121305. [CrossRef]

2.   Keçeciler, A.; Acar, H.İ.; Doğan, A. Thermodynamic analysis of the absorption refrigeration system with geothermal energy: An experimental study. *Energy Convers. Manag.* **2000**, *41*, 37–48. [CrossRef]

3.   Yang, M.; Lee, S.Y.; Chung, J.T.; Kang, Y.T. High efficiency H_2O/LiBr double effect absorption cycles with multi-heat sources for tri-generation application. *Appl. Energy* **2017**, *187*, 243–254. [CrossRef]

4.   Kaynakli, O.; Saka, K.; Kaynakli, F. Energy and exergy analysis of a double effect absorption refrigeration system based on different heat sources. *Energy Convers. Manag.* **2015**, *106*, 21–30. [CrossRef]

5.   Riffat, S.B.; Qiu, G. Comparative investigation of thermoelectric air-conditioners versus vapour compression and absorption air-conditioners. *Appl. Therm. Eng.* **2004**, *24*, 1979–1993. [CrossRef]

6.   Azhar, M.; Siddiqui, M.A. Optimization of operating temperatures in the gas operated single to triple effect vapour absorption refrigeration cycles. *Int. J. Refrig.* **2017**, *82*, 401–425. [CrossRef]

7. Azhar, M.; Siddiqui, M.A. Exergy analysis of single to triple effect lithium bromide-water vapour absorption cycles and optimization of the operating parameters. *Energy Convers. Manag.* **2019**, *180*, 1225–1246. [CrossRef]

8. Karamangil, M.I.; Coskun, S.; Kaynakli, O.; Yamankaradeniz, N. A simulation study of performance evaluation of single-stage absorption refrigeration system using conventional working fluids and alternatives. *Renew. Sustain. Energy Rev.* **2010**, *14*, 1969–1978. [CrossRef]

9. Ahmad, T.; Azhar, M.; Sinha, M.K.; Meraj, M.; Mahbubul, I.M.; Ahmad, A. Energy analysis of lithium bromide-water and lithium chloride-water based single effect vapour absorption refrigeration system: A comparison study. *Clean. Eng. Technol.* **2022**, *7*, 100432. [CrossRef]

10. De Araújo, H.V.; Massuchetto, L.H.P.; do Nascimento, R.B.C.; de Carvalho, S.M.R.; Dangelo, J.V.H. Thermodynamic performance analysis of a single-effect absorption refrigeration system operating with water and 1-ethyl-3-methylimidazolium-based ionic liquids mixtures. *Appl. Therm. Eng.* **2022**, *201*, 117761. [CrossRef]

11. Saravanan, R.; Maiya, M.P. Thermodynamic comparison of water-based working fluid combinations for a vapour absorption refrigeration system. *Appl. Therm. Eng.* **1998**, *18*, 553–568. [CrossRef]

12. Papadopoulos, A.I.; Kyriakides, A.-S.; Seferlis, P.; Hassan, I. Absorption refrigeration processes with organic working fluid mixtures—A review. *Renew. Sustain. Energy Rev.* **2019**, *109*, 239–270. [CrossRef]

13. Qin, Y.; Li, N.; Zhang, H.; Liu, B. Thermodynamic performance of a modified −150 °C refrigeration system coupled with Linde-Hampson and three-stage auto-cascade using low-GWP refrigerants. *Energy Convers. Manag.* **2021**, *236*, 114093. [CrossRef]

14. Ratlamwala, T.A.H.; Dincer, I.; Gadalla, M.A. Performance analysis and evaluation of a triple-effect ammonia-water absorption-refrigeration system. *Int. J. Energy Res.* **2013**, *37*, 475–483. [CrossRef]

15. Hugo, V.; Flores, F.; Román, J.C.; Alpírez, G.M. Performance Analysis of Different Working Fluids for an Absorption Refrigeration Cycle. *Am. J. Environ. Eng.* **2014**, *4*, 1–10.

16. Xu, Z.Y.; Wang, R.Z. Absorption refrigeration cycles: Categorized based on the cycle construction. *Int. J. Refrig.* **2016**, *62*, 114–136. [CrossRef]

17. Talpada, J.S.; Ramana, P.V. A review on performance improvement of an absorption refrigeration system by modification of basic cycle. *Int. J. Ambient. Energy* **2019**, *40*, 661–673. [CrossRef]

18. Ohuchi, T.; Usui, S.; Fukuda, T.N.A. Multistage Absorption Refrigeration System. U.S. Patent 4,520,634, 4 June 1985.

19. Domínguez-Inzunza, L.A.; Hernández-Magallanes, J.A.; Sandoval-Reyes, M.; Rivera, W. Comparison of the performance of single-effect, half-effect, double-effect in series and inverse and triple-effect absorption cooling systems operating with the NH3-LiNO₃ mixture. *Appl. Therm. Eng.* **2014**, *66*, 612–620. [CrossRef]

20. Maryami, R.; Dehghan, A.A. An exergy based comparative study between LiBr/water absorption refrigeration systems from half effect to triple effect. *Appl. Therm. Eng.* **2017**, *124*, 103–123. [CrossRef]

21. Nikbakhti, R.; Wang, X.; Hussein, A.K.; Iranmanesh, A. Absorption cooling systems—Review of various techniques for energy performance enhancement. *Alex. Eng. J.* **2020**, *59*, 707–738. [CrossRef]

22. Arshi Banu, P.S.; Sudharsan, N.M. Review of water based vapour absorption cooling systems using thermodynamic analysis. *Renew. Sustain. Energy Rev.* **2018**, *82*, 3750–3761. [CrossRef]

23. Mouneer, T.A.; Hawwash, A.A.; Aly, M.H.; Mina, E.M. Thermodynamic analysis for novel vapor compression/absorption cascade refrigeration system for LNG liquefaction processes in Egypt. *Energy Convers. Manag.* **2022**, *270*, 116238. [CrossRef]

24. Aghdam, A.H.; Ranjbar, F.; Mahmoudi, S.M.S. Performance comparison of triple-effect parallel flow and series flow absorption refrigeration systems. *J. Appl. Sci.* **2008**, *8*, 2913–2918. [CrossRef]

25. Wang, L.; You, S.; Zhang, H.; Li, X. Simulation of gas-fired triple-effect LiBr/water absorption cooling system with exhaust heat recovery generator. *Trans. Tianjin Univ.* **2010**, *16*, 187–193. [CrossRef]

26. Azhar, M.; Siddiqui, M.A. First and Second Law Analyses of Double Effect Parallel and Series Flow Direct Fired Absorption Cycles for Optimum Operating Parameters. *J. Energy Resour. Technol. Trans. ASME* **2019**, *141*, 124501. [CrossRef]

27. Chahartaghi, M.; Golmohammadi, H.; Shojaei, A.F. Performance analysis and optimization of new double effect lithium bromide–water absorption chiller with series and parallel flows. *Int. J. Refrig.* **2019**, *97*, 73–87. [CrossRef]

28. Konwar, D.; Gogoi, T.K.; Das, A.J. Multi-objective optimization of double effect series and parallel flow water–lithium chloride and water–lithium bromide absorption refrigeration systems. *Energy Convers. Manag.* **2019**, *180*, 425–441. [CrossRef]

29. Bagheri, B.S.; Shirmohammadi, R.; Mahmoudi, S.M.S.; Rosen, M.A. Optimization and comprehensive exergy-based analyses of a parallel flow double-effect water-lithium bromide absorption refrigeration system. *Appl. Therm. Eng.* **2019**, *152*, 643–653. [CrossRef]

30. Morosuk, T.; Tsatsaronis, G. A new approach to the exergy analysis of absorption refrigeration machines. *Energy* **2008**, *33*, 890–907. [CrossRef]

31. Kelly, S.; Tsatsaronis, G.; Morosuk, T. Advanced exergetic analysis: Approaches for splitting the exergy destruction into endogenous and exogenous parts. *Energy* **2009**, *34*, 384–391. [CrossRef]

32. Garousi Farshi, L.; Seyed Mahmoudi, S.M.; Rosen, M.A.; Yari, M. A comparative study of the performance characteristics of double-effect absorption refrigeration systems. *Int. J. Energy Res.* **2012**, *36*, 182–192. [CrossRef]

33. Arshad, M.U.; Ghani, M.U.; Ullah, A.; Güngör, A.; Zaman, M. Thermodynamic analysis and optimization of double effect absorption refrigeration system using genetic algorithm. *Energy Convers. Manag.* **2019**, *192*, 292–307. [CrossRef]

34. Ferwati, M.S.; Ahmad, A.M.; Takalkar, G.D.; Bicer, Y. Energy and exergy analysis of parallel flow double effect H_2O-[mmim][DMP] absorption refrigeration system for solar powered district cooling. *Case Stud. Therm. Eng.* **2021**, *28*, 101382. [CrossRef]

35. Arora, A.; Dixit, M.; Kaushik, S.C. Energy and exergy analysis of a double effect parallel flow $LiBr/H_2O$ absorption refrigeration system. *J. Therm. Eng.* **2016**, *2*, 541–549. [CrossRef]

36. Ahmed, S.; Mohammed, M.S.A.; Ul-Haq Gilani, S.I. Exergy analysis of a double-effect parallel-flow commercial steam absorption chiller. *J. Appl. Sci.* **2012**, *12*, 2580–2585. [CrossRef]

37. Kaneesamkandi, Z.; Almujahid, A.; Salim, B. Selection of an Appropriate Solar Thermal Technology for Solar Vapor Absorption Cooling—An MADM Approach. *Energies* **2022**, *15*, 1882. [CrossRef]

38. Yu, M.; Chen, Z.; Yao, D.; Zhao, F.; Pan, X.; Liu, X.; Cui, P.; Zhu, Z.; Wang, Y. Energy, exergy, economy analysis and multi-objective optimization of a novel cascade absorption heat transformer driven by low-level waste heat. *Energy Convers. Manag.* **2020**, *221*, 113162. [CrossRef]

39. Gado, M.G.; Ookawara, S.; Nada, S.; El-Sharkawy, I.I. Hybrid sorption-vapor compression cooling systems: A comprehensive overview. *Renew. Sustain. Energy Rev.* **2021**, *143*, 110912. [CrossRef]

40. Yu, M.; Cui, P.; Wang, Y.; Liu, Z.; Zhu, Z.; Yang, S. Advanced Exergy and Exergoeconomic Analysis of Cascade Absorption Refrigeration System Driven by Low-Grade Waste Heat. *ACS Sustain. Chem. Eng.* **2019**, *7*, 16843–16857. [CrossRef]

41. Wang, Y.; Liu, Y.; Liu, X.; Zhang, W.; Cui, P.; Yu, M.; Liu, Z.; Zhu, Z.; Yang, S. Advanced exergy and exergoeconomic analyses of a cascade absorption heat transformer for the recovery of low grade waste heat. *Energy Convers. Manag.* **2020**, *205*, 112392. [CrossRef]

42. Kaita, Y. Simulation results of triple-effect absorption cycles. *Int. J. Refrig.* **2002**, *25*, 999–1007. [CrossRef]

43. Azhar, M.; Altamush Siddiqui, M. Comprehensive exergy analysis and optimization of operating parameters for double effect parallel flow absorption refrigeration Cycle. *Therm. Sci. Eng. Prog.* **2020**, *16*, 100464. [CrossRef]

44. Azhar, M.; Siddiqui, M.A. Energy and Exergy Analyses for Optimization of the Operating Temperatures in Double Effect Absorption Cycle. *Energy Procedia* **2017**, *109*, 211–218. [CrossRef]

45. Ansari, K.A.; Azhar, M.; Altamush Siddiqui, M. Exergy Analysis of Single-Effect Vapor Absorption System Using Design Parameters. *J. Energy Resour. Technol.* **2020**, *143*, 062105. [CrossRef]

46. Pátek, J.; Klomfar, J. A computationally effective formulation of the thermodynamic properties of $LiBr$-H_2O solutions from 273 to 500 K over full composition range. *Int. J. Refrig.* **2006**, *29*, 566–578. [CrossRef]

47. Altamush Siddiqui, M. Optimization of Operating Parameters for Various Absorption Systems Using Renewable Energies. Ph.D. Thesis, Aligarh Muslim Univesity, Aligarh, India, 1992.

48. Pátek, J.; Klomfar, J. A simple formulation for thermodynamic properties of steam from 273 to 523 K, explicit in temperature and pressure. *Int. J. Refrig.* **2009**, *32*, 1123–1125. [CrossRef]